In situ forming heterojunction of thiophene-based metal-organic frameworks with carbon dots for efficient overall water splitting and supercapacitor

Qianqian Wang，Xiaoyan Ma, Ran Bi, Xiangpan Hu, Senyang Song, Pengcheng Ma, Fang Chen*

School of Chemistry and Chemical Engineering, Northwestern Polytechnical University, Xi'an 710072, China

* Corresponding author: E-mail: m_xiao_yana@nwpu.edu.cn (X. Ma).

1.1 Characterizations

Crystallographic data for the samples were obtained using a powder X-ray diffractometer (D8 Advance (Germany)) with Cu Kα1 (λ=1.54 Å) source. The Fourier transform infrared (FT-IR) spectra were acquired with Fourier infrared spectroscopy (W QF-310) in 400-4000 cm^{-1}. Raman was tested by Alpha300R with a 532 nm TEM00 laser. The morphology of the materials was characterized using a field-emission scanning electron microscope (SEM, Hitachi Regulus8100), and the elemental composition of the samples was analyzed using an energy-dispersive X-ray spectrometer. Transmission electron microscopy (TEM) images were obtained using JEOL JEM-2100 (100 kV). The materials were analyzed using an X-ray photoelectron spectroscopy (XPS) utilizing Kratos AXIS Ultra DLD (UK). UV-vis diffuse reflectance spectra (UV-vis-DRS) were obtained on a Shimadzu UV-3600 spectrophotometer using $BaSO_4$ as a reflectance standard. The pore structure changes of powder samples were recorded through N_2 adsorption/analytic isotherm curves (BET, 3H-2000PS2) and

small angle neutron scattering (SANS，Chinese Spallation Neutron Source (Dongguan, China)).

1.2 Electrochemical measurements

For electrochemical investigations, electrocatalytic water splitting and supercapacitors were operated with electrochemical workstation (CHI760E). The reference electrode in all three-electrode experiments with 1M KOH was Hg/HgO, while the counter electrode was Pt plate. Electrochemical impedance spectroscopy (EIS) measurements were performed by scanning the frequency from 100 - 0.01 kHz. The double-layer capacitance (C_{dl}) was recorded using the plots of $\frac{\Delta j}{2} = (j_{anode} - j_{cathode})/2$ at a non-faradaic potential against different scan rates (10-100 mV s^{-1}). At a scan rate of 5 mV s^{-1}, linear sweep voltammograms (LSV) in OER and HER were recorded and calculated without iR-correction. Using the Nernst equation, the measured potentials were converted to the reversible hydrogen electrode (RHE) scale: $E(RHE) = E(Hg/HgO) + 0.0592 \times pH + 0.098$. The Tafel curves were obtained from LSV curves based on $\eta = b\log(j) + a$ (b: Tafel slope; η: overpotential; j: current density).

Supercapacitor measurement and calculations: The GCD and CV curves were also tested on electrochemical workstation using 1 M KOH aqueous solution. Moreover, the mass specific capacitance (C_m, F g^{-1}) was calculated according to $C_m = I \times \Delta t_d/(m \times \Delta V)$. Where I is the constant discharge current (A), Δt_d is the discharge time, m is the mass of active material (The amount of active substance contained in each SC-FeNiCeP/NF single side: 0.0049 g), and ΔV is the voltage window. The asymmetric supercapacitors were assembled by using 400N-CDs/FeNi-TDC as positive electrode, AC (which

mixed with carbon black and PTFE with a weight ratio of 8:1:1) coated on nickel foam substrate as negative electrode and 1 M KOH aqueous solution as the electrolyte. The energy density and power density of assembled ASC are calculated based on equation $E = C \times \Delta V^2/(3.6 \times 2)$and $P = 3600 \times E/\Delta t$, respectively. Among them, C is the specific capacitance.

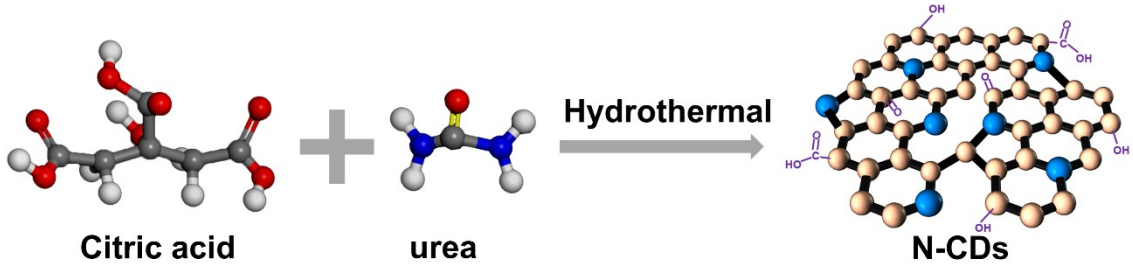

Figure S1. Schematic diagram of the preparation of N-CDs.

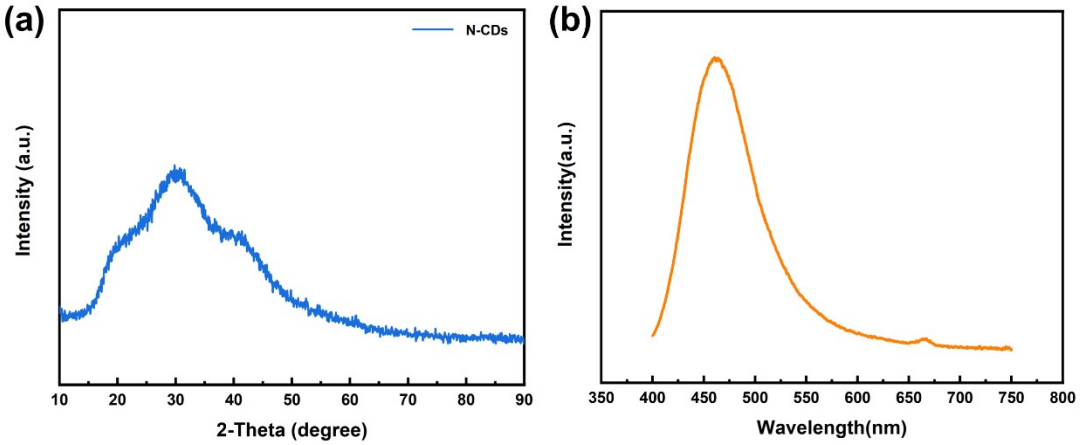

Figure S2. (a) XRD pattern and (b) Excitation-dependent PL of N-CDs.

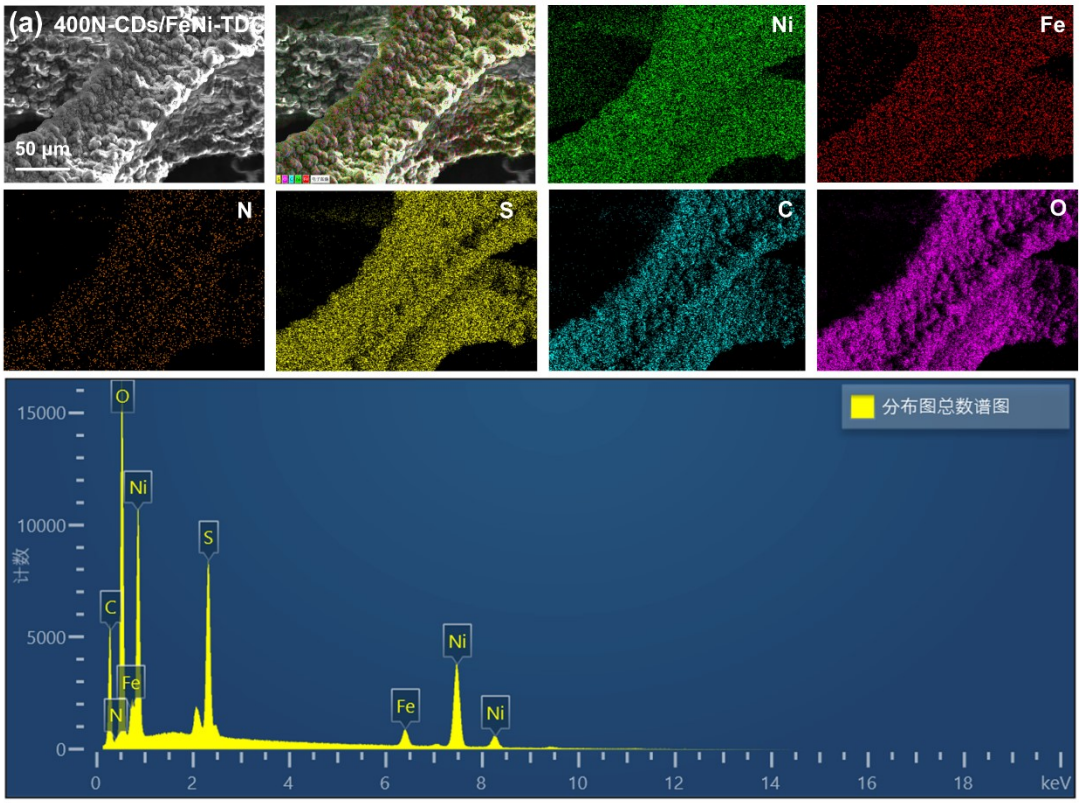

Figure S3. SEM, EDX element mapping and the element content distribution of 400N-CDs/FeNi-TDC.

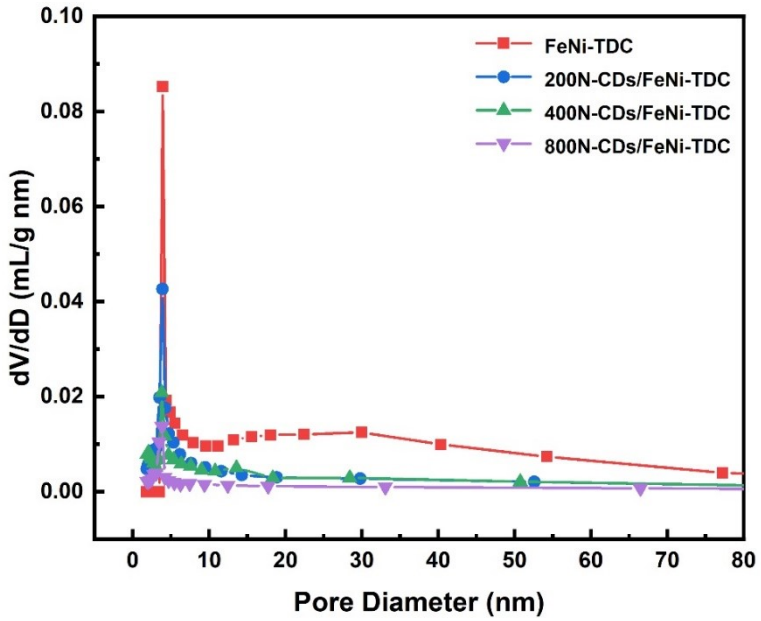

Figure S4. Pore size distribution of FeNi-TDC, 200N-CDs/FeNi-TDC, 400N-CDs/FeNi-TDC and 800N-CDs/FeNi-TDC.

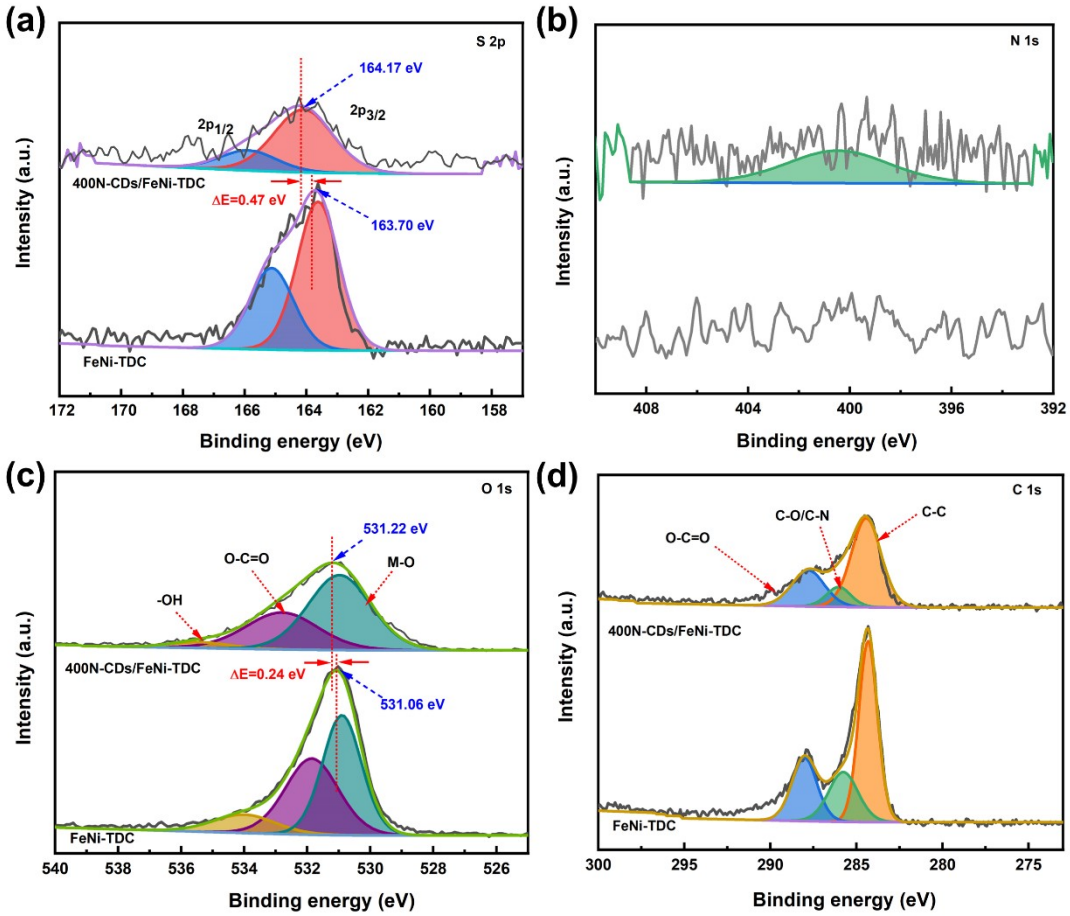

Figure S5. High-resolution XPS spectra of FeNi-TDC and 400N-CDs/FeNi-TDC samples: (a) S 2p; (b) N 2p; (c) O 1s and (d) C 1s.

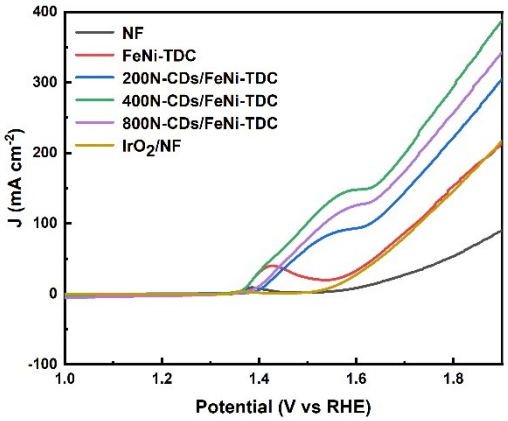

Figure S6. (a) LSV of the FeNi-TDC, 200N-CDs/FeNi-TDC, 400N-CDs/FeNi-TDC, 800N-CDs/FeNi-TDC, IrO_2/NF and NF in OER.

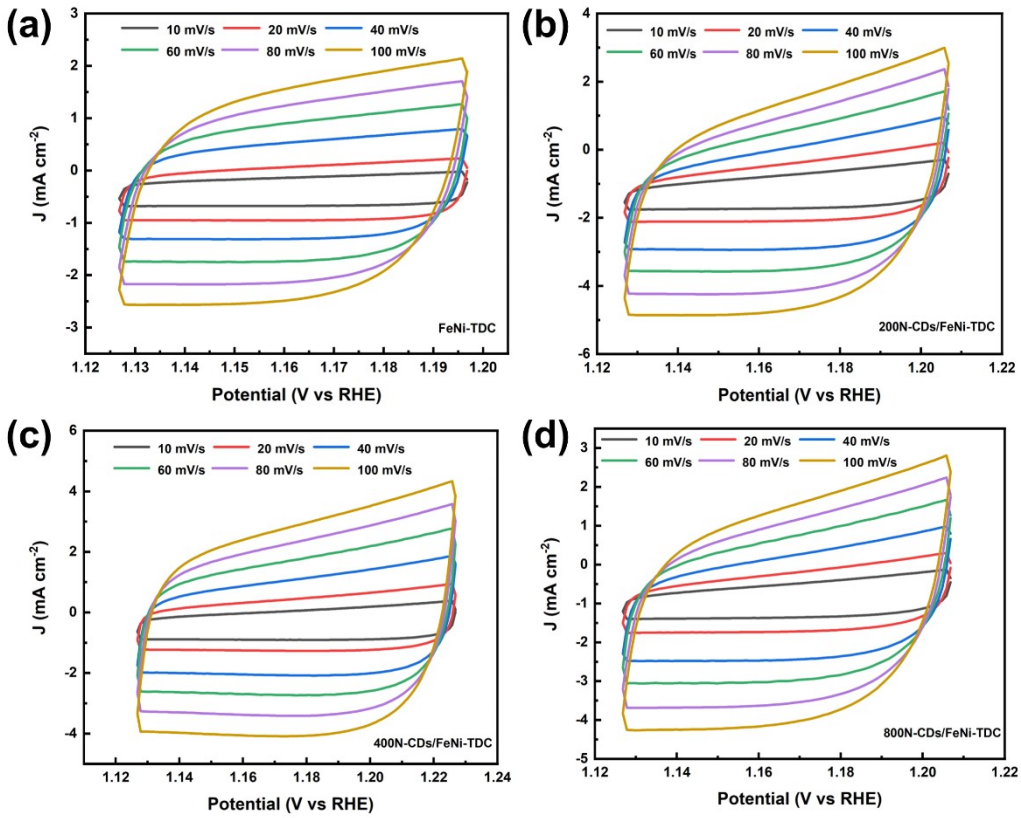

Figure S7. CV curve of as-obtained samples at a scan rate between 10 and 100 mV s^{-1}: (a) FeNi-TDC, (b) 200N-CDs/FeNi-TDC, (c) 400N-CDs/FeNi-TDC and (d) 800N-CDs/FeNi-TDC.

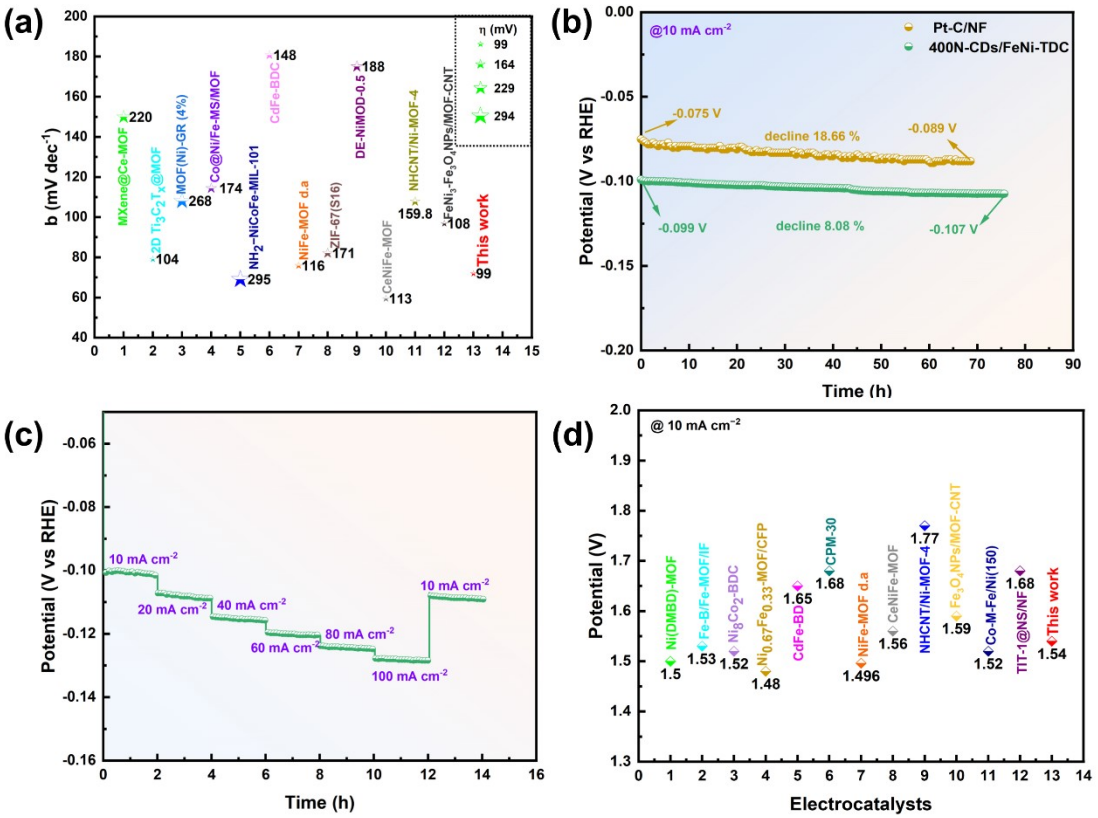

Figure S8. (a) Comparison of overpotential between the 400N-CDs/FeNi-TDC and other recently reported electrocatalysts in HER; (d) V-t curves of 400N-CDs/FeNi-TDC and Pt-C/NF at 10 mA cm^{-2}; (c) Multicurrent steps curve of the 400N-CDs/FeNi-TDC at different current density; (d) Compared with reported applied voltages of OWS.

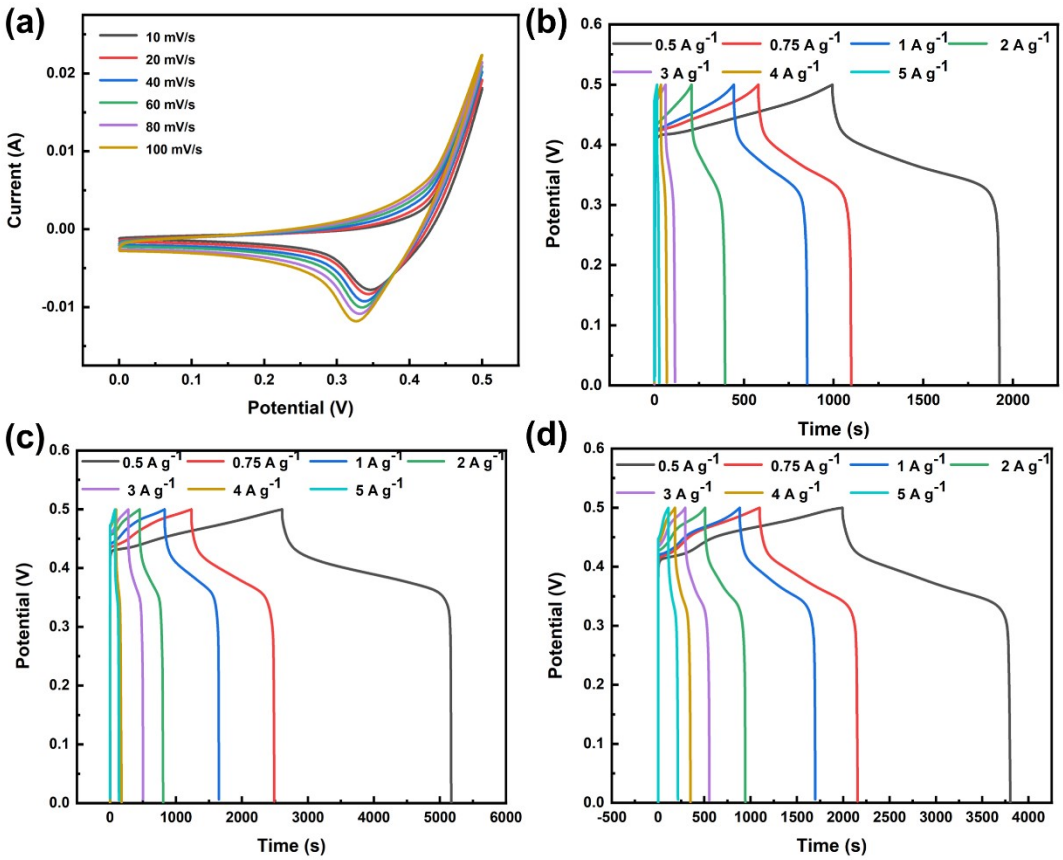

Figure S9. (a) CV curves of 400N-CDs/FeNi-TDC at different scan rates; GCD curves of FeNi-TDC (b); 200N-CDs/FeNi-TDC (c) and 800N-CDs/FeNi-TDC (d).

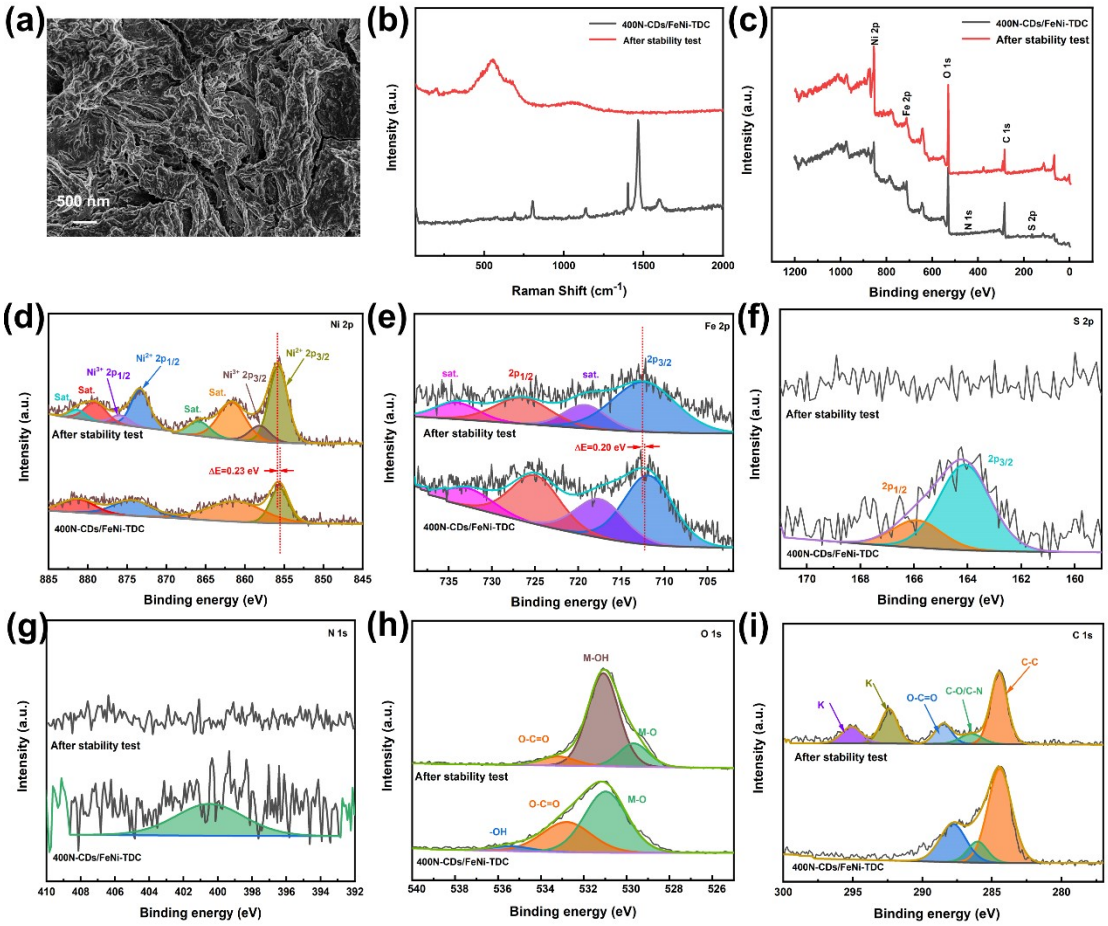

Figure S10. (a) SEM image, (b) Raman of post-OER 400N-CDs/FeNi-TDC; High-resolution XPS spectra of the initial and post-OER 400N-CDs/FeNi-TDC: (c) survey spectra; (d) Ni 2p; (e) Fe 2p; (f) S 2p; (g) N 1s; (h) O 1s and (i) C 1s.

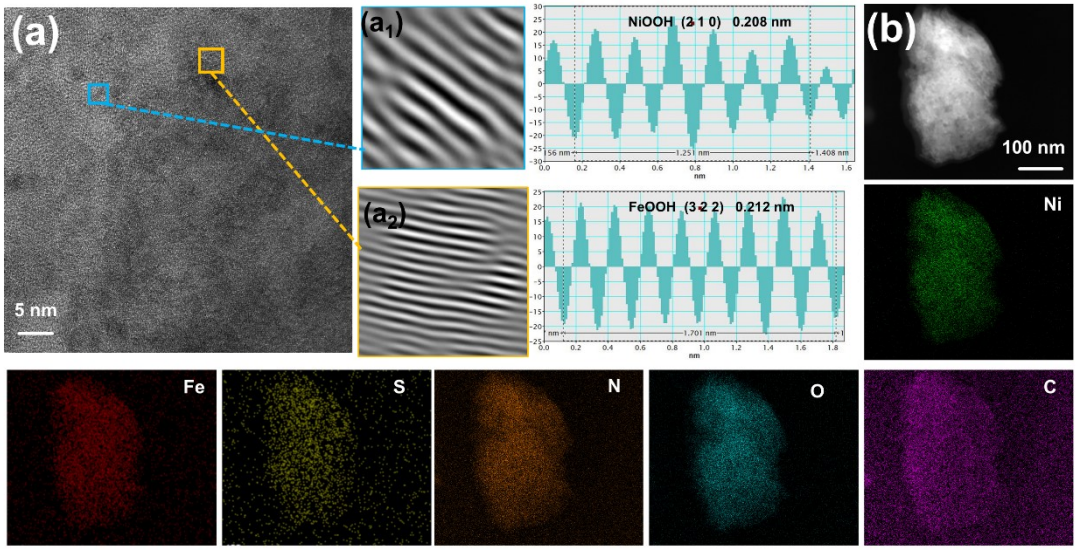

Figure S11. (a) HRTEM; (b) corresponding elemental color mappings of the 400N-CDs/FeNi-TDC after the OER test.

Table S1. A comparison of 400N-CDs/FeNi-TDC electrocatalyst with recently reported catalysts in OER performance

Electrocatalyst	η(mV)	b(mV dec^{-1})	Stability	Ref.
$FeCo_3(DDA)_2$	260 at 10 mA cm^{-2}	46.86	2000h	[1]
CoNiFc-MOF	209 at 10 mA cm^{-2}	39	30h	[2]
Ni(DMBD)-MOF	295 at 10 mA cm^{-2}	32	100h	[3]
$Co[C_6H_6N_4]NO_2$	280 at 10 mA cm^{-2}	33	20h	[4]
NiFe-LDH/MOF	208 at 20 mA cm^{-2}	61	100h	[5]
Fe-B/Fe-MOF/IF	210 at 10 mA cm^{-2}	38	100h	[6]
Ni_8Co_2-BDC	274 at 10 mA cm^{-2}	73.1	48h	[7]
$Ni_{0.67}Fe_{0.33}$-MOF/CFP	281 at 10 mA cm^{-2}	38	80h	[8]
NiFe-MOF/G	258 at 10 mA cm^{-2}	49	30h	[9]
NiFe-MOF NSs@CQDs-COOH	261 at 10 mA cm^{-2}	56	200h	[10]
CoNi MOFs-mCNTs	306 at 10 mA cm^{-2}	42	15h	[11]
Co-ZIF/CDs/CC	226 at 10 mA cm^{-2}	147	24h	[12]
FeNiCo-MIL/Ti_3C_2	231 at 10 mA cm^{-2}	34.5	24h	[13]
MXene@Ce-MOF	270 at 10 mA cm^{-2}	163.8	12h	[14]
CQDs $_{10}$ @NiFe-MOF-A	289 at 10 mA cm^{-2}	52.7	30,000s	[15]
400N-CDs/FeNi-TDC	209 at 10 mA cm^{-2}	18.9	70 h	This work

Table S2. A comparison of 400N-CDs/FeNi-TDC electrocatalyst with recently reported catalysts in HER performance

Electrocatalyst	η(mV)	b (mV dec^{-1})	Stability	Ref.
MXene@Ce-MOF	220 at 10 mA cm^{-2}	149.9	12h	[14]
2D $Ti_3C_2T_x$@MOF	104 at 10 mA cm^{-2}	79	30 h	[16]
MOF(Ni)-GR (4%)	268 at 10 mA cm^{-2}	108	24 h	[17]
Co@Ni/Fe-MS/MOF	174 at 10 mA cm^{-2}	114.35	80 h	[18]
NH_2-NiCoFe-MIL-101	295 at 0.6 A cm^{-2}	69	100 h	[19]
CdFe-BDC	148 at 10 mA cm^{-2}	180.71	60	[20]
NiFe-MOF d.a	116 at 10 mA cm^{-2}	75.8	30 h	[21]
ZIF-67 (S16)	171 at 10 mA cm^{-2}	82	15 h	[22]
DE-NiMOF-0.5	188 at 10 mA cm^{-2}	175	24 h	[23]
CeNiFe-MOF	113 at 10 mA cm^{-2}	59.4	\	[24]
NHCNT/Ni-MOF-4	159.8 at 10 mA cm^{-2}	107.69	50 h	[25]
$FeNi_3$-Fe_3O_4 NPs/MOF-CNT	108 at 10 mA cm^{-2}	96.75	20 h	[26]
400N-CDs/FeNi-TDC	99 mV at 10 mA cm^{-2}	71.01	70 h	This work

Table S3. Summary of various MOF-based electrodes for overall water splitting

Electrocatalyst	Voltage	Stability	Ref.
Ni(DMBD)-MOF	1.50 V@10 mA cm^{-2}	100 h	[3]
Fe-B/Fe-MOF/IF	1.53 V@10 mA cm^{-2}	10 h	[6]
Ni_8Co_2-BDC	1.52 V@10 mA cm^{-2}	48 h	[7]
$Ni_{0.67}Fe_{0.33}$-MOF/CFP	1.48 V @10 mA cm^{-2}	80 h	[8]
CPM-30	1.65 V @10 mA cm^{-2}	40 h	[27]
CdFe-BD	1.68 V@10 mA cm^{-2}	12 h	[20]
NiFe-MOF d.a	1.496 V @10 mA cm^{-2}	30 h	[21]
CeNiFe-MOF	1.56 V @10 mA cm^{-2}	200 h	[24]
NHCNT/Ni—MOF-4	1.77 V @10 mA cm^{-2}	\	[25]
Fe_3O_4 NPs/MOF-CNT	1.59 V @10 mA cm^{-2}	20 h	[26]
Co-M-Fe/Ni(150)	1.52 V @10 mA cm^{-2}	24 h	[28]
TIT-1@NS/NF	1.68 V @10 mA cm^{-2}	16 h	[29]
400N-CDs/FeNi-TDC	1.54 V @ 10 mA cm^{-2}	50 h	This work

Table S4. Summary of various MOF-based electrocatalyst for supercapacitor.

ACS devices	Operating voltage	Energy density	Power density	Ref.
E-NCT MOF//AC	1.5 V	29.34 Wh kg^{-1}	377.27 W kg^{-1}	[30]
Ni-Co PyMOF//AC	1.5 V	37.43 Wh kg^{-1}	850.02 W kg^{-1}	[31]
Cu-PyAc-Am2Ac-Ni // AC	1.5 V	58.95 Wh kg^{-1}	747.25 W kg^{-1}	[32]
CPM-10//AC	1.5 V	15.55 Wh kg^{-1}	750 W kg^{-1}	[27]
MOF8:2//rGO	1.6 V	40 Wh kg^{-1}	800 W kg^{-1}	[33]
MOF@HsGDY//AC	1.6 V	43.3 Wh kg^{-1}	807.6 W kg^{-1}	[34]
N-GLC/MOF-74//AC	1.5 V	52.5 μWh cm^{-2}	0.75 mW cm^{-2}	[35]
400N-CDs/FeNi-TDC||AC	1.5 V	60.63 Wh kg^{-1}	750 W kg^{-1}	This work

References

[1] Lin, L.; Zhang, C.; Liang, C.; Zhang, H.; Wang, Z.; Wang, P.; Zheng, Z.; Cheng, H.; Xing, D.; Dai, Y.; Huang, B.; Liu, Y. Hydrogen bonds induced ultralong stability of conductive π-d conjugated $FeCo_3(DDA)_2$ with high OER activity. *Adv. Mater.* **2024,** *36* (30), 2402388.

[2] Hu, J.; Xu, Q.; Wang, X.; Huang, X.; Zhou, C.; Ye, Y.; Zhang, L.; Pang, H. Charge-transfer-regulated bimetal ferrocene-based organic frameworks for promoting electrocatalytic oxygen evolution. *Carbon Energy.* **2023,** *5* (6), 315.

[3] Liu, Y.; Li, X.; Zhang, S.; Wang, Z.; Wang, Q.; He, Y.; Huang, W. H.; Sun, Q.; Zhong, X.; Hu, J.; Guo, X.; Lin, Q.; Li, Z.; Zhu, Y.; Chueh, C. C.; Chen, C. L.; Xu, Z.; Zhu, Z. Molecular engineering of metal-organic frameworks as efficient electrochemical catalysts for water oxidation. *Adv. Mater.* **2023,** *35* (22), 2300945.

[4] Wang, H.; Gu, M.; Huang, X.; Gao, A.; Liu, X.; Sun, P.; Zhang, X. Ligand-based modulation of the electronic structure at metal nodes in MOF to promote oxygen evolution reaction. *Journal of Materials Chemistry A.* **2023,** *11*, 7239-7245.

[5] Xiao, M.; Wu, C.; Zhu, J.; Zhang, C.; Li, Y.; Lyu, J.; Zeng, W.; Li, H.; Chen, L.; Mu, S. In situ generated layered NiFe-LDH/MOF heterostructure nanosheet arrays with abundant defects for efficient alkaline and seawater oxidation. *Nano Research.* **2023,** *16*, 8945-8952.

[6] Zhao, S.; Deng, L.; Xiong, Y.; Hu, F.; Yin, L.; Yu, D.; Li, L.; Peng, S. Engineering metal-organic framework nanosheets with electronically modulated in-

plane heterojunctions for robust high-current-density water splitting. *Science China Materials.* **2023,** *66* (4), 1373-1382.

[7] Zhou, J.; Qiao, F.; Ren, Z.; Hou, X.; Chen, Z.; Dai, S.; Su, G.; Cao, Z.; Jiang, H.; Huang, M. Amorphization engineering of bimetallic metal-organic frameworks to identify volcano-type trend toward oxygen evolution reaction. *Adv. Funct. Mater.* **2023,** *34* (1), 2304380.

[8] Zhang, S.; Huang, Z.; Isimjan, T. T.; Cai, D.; Yang, X. Accurately substituting Fe for Ni2 atom in Ni-MOF with defect-rich for efficient oxygen evolution reaction: Electronic reconfiguration and mechanistic study. *Applied Catalysis B: Environmental.* **2024,** *343*, 123448.

[9] Wang, Y.; Liu, B.; Shen, X.; Arandiyan, H.; Zhao, T.; Li, Y.; Garbrecht, M.; Su, Z.; Han, L.; Tricoli, A.; Zhao, C. Engineering the activity and stability of MOF-nanocomposites for efficient water oxidation. *Advanced Energy Materials.* **2021,** *11* (16), 2003759.

[10] Song, D.; Guo, H.; Huang, K.; Zhang, H.; Chen, J.; Wang, L.; Lian, C.; Wang, Y. Carboxylated carbon quantum dot-induced binary metal-organic framework nanosheet synthesis to boost the electrocatalytic performance. *Mater. Today.* **2022,** *54*, 42-51.

[11] Yu, S.; Wu, Y.; Xue, Q.; Zhu, J.-J.; Zhou, Y. A novel multi-walled carbon nanotube-coupled CoNi MOF composite enhances the oxygen evolution reaction through synergistic effects. *Journal of Materials Chemistry A.* **2022,** *10* (9), 4936-4943.

[12] Hong, Q.; Wang, Y.; Wang, R.; Chen, Z.; Yang, H.; Yu, K.; Liu, Y.;

Huang, H.; Kang, Z.; Menezes, P. W. In situ coupling of carbon dots with Co-ZIF nanoarrays enabling highly efficient oxygen evolution electrocatalysis. *Small.* **2023,** *19* (31), 2206723.

[13] Nazari, M.; Morsali, A. Trimetallic-organic framework/MXene composite as an oxygen evolution reaction electrocatalyst with elevated intrinsic activity. *Journal of Materials Chemistry A.* **2024,** *12* (8), 4826-4834.

[14] Li, S.; Chai, H.; Zhang, L.; Xu, Y.; Jiao, Y.; Chen, J. Constructing oxygen vacancy-rich MXene @Ce-MOF composites for enhanced energy storage and conversion. *J. Colloid Interface Sci.* **2023,** *642*, 235-245.

[15] Mou, Q.; Wang, X.; Xu, Z.; Zul, P.; Li, E.; Zhao, P.; Liu, X.; Li, H.; Cheng, G. A synergy establishment by metal-organic framework and carbon quantum dots to enhance electrochemical water oxidation. *Chin. Chem. Lett.* **2022,** *33* (1), 562-566.

[16] Zhao, Y.; Wang, S.; Zhang, Z.; Hu, Y.; Ge, K.; Liu, B.; Yang, Y. Effect of electron transfer of 2D $Ti_3C_2T_x$@MOF heterostructure on hydrogen evolution reaction activity. *Int. J. Hydrogen Energy.* **2024,** *55*, 225-233.

[17] Dao, X.; Nie, M.; Sun, H.; Dong, W.; Xue, Z.; Li, Q.; Liao, J.; Wang, X.; Zhao, X.; Yang, D.; Teng, L. Electrochemical performance of metal-organic framework MOF(Ni) doped graphene. *Int. J. Hydrogen Energy.* **2022,** *47* (38), 16741-16749.

[18] Yu, S.; Zhang, N.; Li, J.; Yin, J.; Wang, Y.; Wu, Z.; Zhang, Y.; Du, Y. NiFe-based semi-MOF embedded by sulfide particles reconstructed a three-layer

sandwich structure for alkaline overall water splitting. *ACS Sustainable Chemistry & Engineering.* **2024,** *12* (11), 4551-4564.

[19] Tran, N. Q.; Le, Q. M.; Tran, T. T. N.; Truong, T.-K.; Yu, J.; Peng, L.; Le, T. A.; Doan, T. L. H.; Phan, T. B. Boosting urea-assisted natural seawater electrolysis in 3D leaf-like metal-organic framework nanosheet arrays using metal node engineering. *ACS Applied Materials & Interfaces.* **2024,** *16* (22), 28625-28637.

[20] Luo, Y.; Yang, X.; He, L.; Zheng, Y.; Pang, J.; Wang, L.; Jiang, R.; Hou, J.; Guo, X.; Chen, L. Structural and electronic modulation of iron-based bimetallic metal-organic framework bifunctional electrocatalysts for efficient overall water splitting in alkaline and seawater environment. *ACS Applied Materials & Interfaces.* **2022,** *14* (41), 46374-46385.

[21] Dai, B.; Wei, X.; Chen, L.; Bao, X.; Zhong, Q.; Qu, H. Introducing different long-chain flexible ligands to regulate the transformation behavior of NiFe-MOF and as bifunctional catalysts for the HER/OER. *J. Colloid Interface Sci.* **2025,** *682*, 80-93.

[22] Amirpoor, S.; Dolati, A. Boosting HER performance of ZIF-67 via optimizing synthesis parameters in alkaline medium. *Int. J. Hydrogen Energy.* **2024,** *84*, 14-27.

[23] Wang, N.; Shan, S.; Huang, L.; Zhang, X.; Shu, Z.; Zhang, Q.; Xu, Y.; Chen, J.; Yang, J. Application and performance Enhancement of acetic acid-Regulated ligand defect engineering in NiMOF electrocatalysts. *Int. J. Hydrogen Energy.* **2024,** *94*, 456-463.

[24] Yang, J.; Shen, Y.; Xian, J.; Xiang, R.; Li, G. Rare-earth element doped NiFe-

MOFs as efficient and robust bifunctional electrocatalysts for both alkaline freshwater and seawater splitting. *Chemical Science.* **2025,** *16*, 685-692.

[25] Bhosale, M.; Murugan, N.; Kim, Y. A.; Thangarasu, S.; Oh, T. H. Interface engineering of network‐like 1D/2D (NHCNT/Ni-MOF) hybrid nanoarchitecture for electrocatalytic water splitting. *Small Methods.* **2024**, 2401492.

[26] Srinivas, K.; Lu, Y.; Chen, Y.; Zhang, W.; Yang, D. $FeNi_3$-Fe_3O_4 Heterogeneous Nanoparticles Anchored on 2D MOF Nanosheets/1D CNT Matrix as Highly Efficient Bifunctional Electrocatalysts for Water Splitting. *ACS Sustainable Chemistry & Engineering.* **2020,** *8* (9), 3820-3831.

[27] Han, Y.; Liu, Z.; Wang, C.; Guo, L.; Wang, Y. Construction of rod-like cobalt-pyridinedicarboxylic acid/MXene nanosheets composites for hydrogen evolution reaction and supercapacitor. *J. Colloid Interface Sci.* **2024,** *661*, 139-149.

[28] Chen, P.; Duan, X.; Li, G.; Qiu, X.; Wang, S.; Huang, Y.; Stavitskaya, A.; Jiang, H. Construction of ZIF-67/MIL-88(Fe, Ni) catalysts as a novel platform for efficient overall water splitting. *Int. J. Hydrogen Energy.* **2023,** *48* (20), 7170-7180.

[29] Zhang, J.; Zong, S.; Xiong, G.; Lin, B.; Lv, J.; Xiao, N.; Zhao, H.; Gui, L.; Guo, X.; Liu, X. Ultrathin 2D metal-organic framework nanosheet arrays to boost the overall efficiency of water splitting. *Int. J. Hydrogen Energy.* **2024**. https://doi.org/10.1016/j.ijhydene.2024.06.162.

[30] Song, S.; Ma, X.; Zhang, B.; Li, W.; Feng, Y.; Tan, C. Morphologies of thienyl based bimetallic metal-organic frameworks controlled by solvents for high specific capacitance supercapacitor. *Journal of Energy Storage.* **2022,** *47*, 103627.

[31] Sun, J.; Song, S.; Deng, C.; Wang, Q.; Ma, X. Enhancing energy storage and catalytic properties of bimetallic multifunctional MOFs by designing secondary-building units. *Journal of Energy Storage.* **2024,** *94*, 112288.

[32] Song, S.; Sun, J.; Deng, C.; Wang, Q.; Ma, X. Ligand regulation and capacitive properties of nickel based pyrazole trinuclear copper cluster organic framework. *Colloids and Surfaces A: Physicochemical and Engineering Aspects.* **2024,** *694*, 134052.

[33] Huang, S.; Shi, X.-R.; Sun, C.; Zhang, X.; Huang, M.; Liu, R.; Wang, H.; Xu, S. Template-controlled in-situ growing of NiCo-MOF nanosheets on Ni foam with mixed linkers for high performance asymmetric supercapacitors. *Appl. Surf. Sci.* **2022,** *572*, 151344.

[34] Abbas, Z.; Hussain, N.; Mobin, S. M. Crumpled fibrous graphdiyne network decorated metal-organic framework: a promising heterostructure for improved energy storage performance. *Journal of Materials Chemistry A.* **2024,** *12* (31), 20170-20178.

[35] Feng, W.; Liu, C.; Liu, Z.; Pang, H. In-situ growth of N-doped graphene-like carbon/MOF nanocomposites for high-performance supercapacitor. *Chin. Chem. Lett.* **2024,** *35* (12), 109552.